SSC21-WKIV-05

Design of an Imaging Payload for Earth Observation from a Nanosatellite

Elliot Saive[1], Liam Droog[2], Katelyn Ball[2], Jari Swanson[1], Elizabeth Chao[3], Michael G. Lipsett[3], Amina E. Hussein[1], Carlos F. Lange[3], Bruce F. Cockburn[1], Duncan G. Elliott[1],
[1]Department of Electrical and Computer Engineering, University of Alberta,
[2]Department of Physics, University of Alberta,
[3]Department of Mechanical Engineering, University of Alberta
Edmonton, Alberta, Canada; 780-318-2129
esaive@ualberta.ca

ABSTRACT

A compact imaging payload consisting of visible-near infrared and short-wave infrared capability is being developed to demonstrate low-cost wildfire monitoring among other Earth observations. Iris is a 1U multispectral push-broom imager that is capable of generating spectral data pertinent for wildfire science and wildfire risk analysis from a CubeSat platform. This payload is slated to fly on-board Ex-Alta 2, the University of Alberta's second CubeSat and Alberta's contribution to the Canadian CubeSat Project, to be deployed from the International Space Station in 2022. Iris features four closely integrated designs: optical, structural, electronics, and firmware. The mechanical and electronic interfaces of Iris are suited for modular integration into 1U of other generic CubeSat structures.

The design has significant constraints on mass, size, performance, and cost. The current optical design features two compact lightpaths within the housing for imaging in short-wave infrared, near-infrared, blue, and red bands (center wavelengths at 2100, 865, 490, and 665 nm, respectively). Design simulations suggest achievement of a signal-to-noise ratio greater than 20 dB across all bands and a spatial resolution of 360 m or better averaged across the field-of-view. Taken together, this demonstrates significant scientific value for minimized cost and instrument volume. This design uses exclusively commercially available lenses, providing significant overall cost savings.

The structural housing of Iris consists of 6061 T6 Aluminum, which provides a light-tight optical path for the visible to near-infrared and short-wave infrared light paths, as well as mounting for the optics and printed circuit board to the CubeSat structure within the required tolerances. A 45-degree folding mirror is employed to provide an extended optical lightpath within 1U with no deployable optics. The lens and mirror mounts are fitted with manual adjustment mechanisms for post-assembly alignment of the optical elements. This feature allows the team to perform small modifications to the axial position of the lenses as well as the folding mirror plane without having to re-manufacture the structure, saving time and cost.

Within Iris, a subsystem named Electra features a custom filtered CMV4000 CMOS detector from *ams AG* integrated alongside a custom filtered G11478-512WB InGaAs linear array from *Hamamatsu*. Electra is a custom printed circuit board which houses an Intel Cyclone V system-on-chip field-programmable gate array, 512 MB of DDR3 synchronous dynamic random-access memory, and other supporting infrastructure for controlling Iris imaging operations and handling spectral data. An in-house software and VHDL suite is implemented within Electra for sensor control, memory management, and all off-board communications. Software functionality includes data compression and a cloud detection algorithm, wherein images are ranked based on heuristic value of relative cloud content, together increasing scientific value per spacecraft link time.

A full proto-flight model of Iris is scheduled for manufacturing and testing in Q4 2021. Following manufacturing, comprehensive validation analysis and characterization will be performed, confirming ability to meet mission requirements.

INTRODUCTION

Ex-Alta 2 is a three-unit (3U) CubeSat, where 1U is a cube of approximately $10 \times 10 \times 10$ cm. CubeSats are characterized by reduced cost and heightened modularity when compared to traditional spacecraft; as a result, CubeSats have become popular for both commercial and academic purposes.[1] Ex-Alta 2 is Alberta's contribution to the Canadian CubeSat project, and is currently being designed, constructed, and tested by students at the University of Alberta in Edmonton, Alberta.

Ex-Alta 2 carries an imaging payload called Iris, which gathers multispectral images in four distinct wavelength bands pertinent for wildfire monitoring, research, and risk mitigation using a pushbroom orbital imaging technique. Iris occupies 1U of the spacecraft and features a compact modular design to facilitate integration into other CubeSat platforms after its first flight aboard Ex-Alta 2.

Figure 1: Render of Ex-Alta 2 in flight configuration.[2]

Wildfire Science Spectra

Normalized Difference Vegetation Index (NDVI) is a common spectral index for characterizing properties of observed vegetation, which utilizes bands with ranges in the approximate regions 600 nm and 800 nm (red and near-infrared [NIR], respectively).[3] NDVI is given by:

$$NDVI = \frac{NIR - R}{NIR + R}$$

where NIR and R are reflectances in near-infrared and red, respectively.

NDVI is useful for characterizing health of vegetation, particularly as it relates to drought conditions, which has implications in monitoring at-risk zones for wildfires.[4] Further, since the red and NIR reflectances differ more widely in vegetation than in soils, NDVI is useful for distinguishing vegetation against underlying soil.[5] The effect of underlying soil on spectral data can be further mitigated via the Soil Adjusted Vegetation Index (SAVI), which is given by:

$$SAVI = \frac{(1 + L)(NIR - R)}{NIR + R + L}$$

where L is an optimized adjustment factor.[6] In addition to NIR and red reflectance, reflectance data in the blue range (approximately 450 - 520 nm) is useful for reducing impact of environmental factors such as atmospheric effects, as well as additional soil background mitigation.[7] One way to utilize blue reflectance data is via the Enhanced Vegetation Index (EVI):

$$EVI = G \cdot \frac{(NIR - R)}{NIR + C_1 R - C_2 B + L}$$

where G, C_1, and C_2 are other optimized correction factors.[7] Further, blue reflectance data can help distinguish smoke from other obstructions such as clouds, vegetation, or other atmospheric effects.[8]

Lastly, short-wave infrared (SWIR) reflectance data (approximately 2000 - 2300 nm) is useful for characterizing the extent of burn damage after a fire, or to penetrate smoke or cloud cover in order to monitor active fires, especially at night. SWIR is also sometimes called mid-infrared (MIR).[9] Combined with NIR reflectance data, SWIR can be used to develop the Normalized Burn Ratio (NBR) of a burned area, which can be determined by exploiting differences in reflectance between NIR and SWIR. The index is given by:

$$NBR = \frac{(NIR - SWIR)}{NIR + SWIR}.$$

In order to best characterize the impacts of wildfires, often the Differenced Normalized Burn Ratio (dNBR) is used, which can more accurately determine post-burn effects relative to the pre-burn conditions:

$$dNBR = NBR_{prefire} - NBR_{postfire}.$$[9]

The indices described above served as primary motivators in the selection of the four bands in which Iris will produce images, as the indices are useful across wildfire science and wildfire risk mitigation.

OPTICS

The optical subsystem of Iris was designed in-house in alignment with AlbertaSat's open-source ethos. Relevant to the development of the optics, performance requirements are defined as follows:

- Spatial resolution shall be smaller than 500 meters;
- Images shall have a Signal-to-Noise (SNR) ratio of at least 20 db;
- Images shall have a radiometric resolution of greater than 8 bits per pixel; and,
- Images shall be spectral measurements which are relevant for NDVI phenology, smoke coverage algorithms, and post-burn analysis.

These are towards one of Ex-Alta 2's Mission Objectives, which is to produce an image that allows scientists to make observations about wildfires. The Iris imaging payload achieves this by gathering both visible and near-infrared (VNIR) and SWIR light.

Optical Configurations

Many well-known optical configurations were explored as potential configurations for Iris, including Newtonian, Cassegrain, and other reflective telescope types. Due to the multi-band nature of our mission requirements and objectives combined with constraints imposed by the compact form factor of the payload, a design was chosen wherein all focusing elements over two distinct lightpaths are purely refractive. Each lightpath has one reflective element in the form of a planar folding mirror, but it serves no purpose other than to lengthen the available lightpath.

Fully custom refractive designs were explored and simulated in Zemax OpticStudio, which included both spherical and aspherical components across multiple iterations. However, custom options were found to be significantly higher in cost than commercial-off-the-shelf (COTS) components, and would not be in the spirit of accessible open-source design work. Hence, COTS designs were developed, and are presented below.

Design Overview

Iris features a dual-aperture design. One lightpath is designed exclusively for SWIR light (approximately 2000–2200 nm), and one is designed for VNIR light, which captures reflectance data in three distinct bands of blue (approximately 465–515 nm), red (approximately 650–680 nm), and near-infrared (approximately 845–885 nm). Splitting of the optical system into two distinct lightpaths yields better performance from each band compared to a single aperture design due to vastly differing sensor form factors, optical transmission properties, filtering requirements, and other optical parameters pertaining to each individual lightpath. COTS spherical optics were chosen to balance performance requirements with financial risk that would follow custom-ground lenses instead of COTS.

In addition to original design of the focusing element set-up, a custom filtering implementation was devised in order to capture all desired wavelength bands. For the VNIR reflectance data, a custom "butcher-block" filter with three separate filtering zones corresponding to our chosen bands was designed and is overlaid atop the chosen VNIR sensor for readout of specific pixel lines in particular bands. For SWIR, a simple custom filter for our desired band is utilized. A more thorough description of the sensor choice, filtering implementation, and image readout process is given later in the report in discussion pertaining to the Iris electronics.

Exposure Analysis

Intrinsic to the design of Iris' optical suite were calculations pertaining to the level of pixel exposure for a given aperture and effective focal length; such considerations were crucial in early trades of competing optical configurations. In this design, calculations provided by Villefranca et al. are used to obtain the SNR of a single pixel for each equipped sensor.[10] The SNR is calculated by obtaining the number of electrons generated by a pixel from a variety of sensor parameters such as quantum efficiency and pixel pitch, as well as well as light intensity factors which consider transmission losses through optics and atmosphere. Ultimately, the shot-noise SNR of a pixel is computed via:

$$SNR = \frac{e^-_{collected}}{\sqrt{e^-_{collected}}}. \tag{1}$$

However, dark current and readout noise can also be accounted for in order to get a more accurate

estimate for SNR per pixel:

$$SNR = \frac{\nu N_\gamma t_{exp}}{\sqrt{\nu N_\gamma t_{exp} + \sigma_D^2 + \sigma_B^2 + \sigma_s^2}},^{11} \quad (2)$$

where:

- $\sigma_s = \sqrt{s}$:
  Photon shot noise, where $s = \nu N_\gamma t_{exp}$. Here, ν is the quantum efficiency, N_γ is the number of photons per pixel per unit time, and t_{exp} is the exposure time.
- $\sigma_D = \sqrt{D}$:
  Dark current shot noise, where $D = i_D t_{exp}$ and i_D is the dark current in electrons per pixel per second.
- $\sigma_B = \sqrt{B}$:
  Background shot noise, where $B = \nu n_B t_{exp}$ and n_B is the number of background photons per pixel per second.

Multiple combinations of effective focal length (EFL) and aperture sizes were tested to compare exposure levels under various constraints for both VNIR and SWIR. To calculate the per-pixel exposure, we utilize code which employs equations from Villafranca et al.[10] An example calculation of exposure for blue light is shown below, along with a table of key results for both VNIR and SWIR lightpaths (Table 2).

Exposure Analysis - Example Calculation

First, the parameters listed in Table 1 are researched and then put into the aforementioned code to obtain our expected per-pixel exposure. Note that each value listed in Table 1 is specific to the wavelength band also listed.

Then, performing these calculations and utilizing other known constants and solar parameters, we obtain a value for the displaced electrons per integration time for this particular band (blue, in this case):

$e^-/\text{pixel}/\text{t}_{\text{int}} = 1249.$

Thus, since the detector has a full-well capacity of 13.5 ke$^-$ per pixel, and with a detector gain setting increasing the electron output by a factor of 3.2, we compute a nominal exposure of approximately 29.6% of the full-well. For a 10-bit detector, we can approximate this as reaching 9-bit resolution since maximum nominal exposure will reach the ninth least significant bit. Further, based on EFL, orbital height, pixel pitch, and orbital velocity, we can compute the integration time for one pixel as:

$$\text{t}_{\text{int}} = \frac{\text{Px} \cdot h}{\text{EFL} \cdot v_g} \quad (3)$$

where Px is the detector pixel pitch, h is the orbital altitude, EFL is still the effective focal length, and v_g is the orbital velocity.

Table 1: Example parameters for optical exposure analysis

Parameter	Value	Description
Wavelength band [nm]	465 - 515	blue band chosen for custom filter implementation.
Altitude [km]	400	Standard assumption for starting height of spacecraft in ISS orbit.
EFL [mm]	85	EFLs explored range from 80 mm to 115 mm.
Aperture [mm]	30	Aperture of available COTS primary lens is 30 mm.
Pixel pitch [µm]	5.5	Pixel pitch of chosen detector (see **Electronics** below).
Quantum efficiency	0.59	Sensor specification.[12]
Transmission of filters	0.95	Custom filter specification.
Transmission of atmosphere	0.55	Lowest value within band range derived from MODTRAN Demo plot.[13]
Transmission of optics	0.62	Computed in Zemax OpticStudio.
Ground reflectivity	0.07	Conifer reflectance in chosen wavelength.[14]
Dark noise [e^-_{rms}]	13	Sensor specification.[12]
Dark current [e^-/s]	125	Sensor specification.[12]

Using this value, we can compute the SNR using Equation (2). For this example, we find:

$\text{SNR}_{1\text{ line}} = 15.5\,\text{dB},$

which does not meet the requirement specified above. Thus, in the Iris electronics back-end (discussed below), we must combine the signals of rows of the same band over the same ground area, where SNR increases by the square root of the number of lines combined, yielding:

$\text{SNR}_{10\text{ lines}} = 20.5\,\text{dB},$

which does meet the requirement.

Table 2 shows the results for this same analysis for all bands and at expected beginning-of-life

(BOL) and near end-of-life (EOL) altitudes. Recall that the values in Table 1 vary by wavelength, hence the values in Table 2 change for each band. Note also that the SNR values listed are sensitive to changes in the amount of pixel-value averaging for a given band for a given image; as mentioned, the number of rows averaged for a given ground area of the same band increases SNR, and is configurable to higher or lower numbers of rows in orbit.

Table 2: Computed exposure and SNR values across expected mission data profile at 89 mm EFL

	400 km		300 km	
Band [nm]	SNR [dB]	Exposure [%]	SNR [dB]	Exposure [%]
650 - 680	20.2	21.9	20.1	16.0
465 - 515	20.3	27.5	20.0	20.1
845 - 885	23.7	100	23.0	95.4
2000 - 2100	22.8	62.1	22.1	45.5

For the VNIR bands, the red and blue bands show lowest exposure, and require pixel averaging of between 10 and 16 rows, respectively, for a given ground area in order to achieve 20 dB SNR. This is due primarily to low vegetation reflectance factors for these bands compared to NIR. For each VNIR band, however, the exposure is adequate such that at least 8 bits of the 10-bit analog-to-digital converter (ADC) on the sensor is utilized between minimum and maximum illumination. For SWIR, the SNR for a single pixel was required to be above 20 dB inherently since pixel averaging for a single ground area is not available with a strictly linear array detector; our design was sufficient for meeting this requirement. Further, with assistance from a configurable on-chip amplifier, the exposure is also adequate, with 45.5% depletion equating to using most bits of the chosen 16-bit ADC.

Resolution Estimates

From a purely geometric standpoint, assuming that the sensor is directly nadir facing and that the ground below is perfectly orthogonal to its local zenith, we can calculate the ground sample distance (GSD) of one pixel:

$$\text{GSD} = \frac{\text{Px} \cdot h}{\text{EFL}}. \tag{4}$$

Note that GSD is derived purely from fundamental optical system parameters, and is not necessarily a measure of system resolution since it does not take into account any aberrations arising from the system. Below details a procedure researched and developed for estimating system resolution based on outputs from optical system design software.

Within Zemax OpticStudio, we can quantify the root mean square (RMS) radius of focused light incident on the image plane for any given system. This serves as a means to calculate the theoretical resolution of an optical system across the entire field-of-view (FOV) of the image plane. To check whether an image will meet the resolution requirement across the FOV, the largest RMS radius across the image plane is used to compute a more accurate representation of system resolution than GSD, which is based on an article by R.R. Auelmann.[15] Note that in the analysis, we first find system resolution in line pairs per mm (lp/mm), and then convert that to units of metres on the ground from orbital height. A derivation of an estimated system resolution based on Zemax OpticStudio simulation is as follows: First, compute the line pairs per millimeter resolution, R, in the image sensor plane, which assumes a diffraction limited case:

$$R_{sensor} = \frac{1}{\text{Px} \cdot 2 \cdot 10^{-3}}. \tag{5}$$

Then, compute the resolution of the image plane based solely on optics by replacing the value for the pixel pitch with the RMS radius of the point spread function of focused light, which is a standard simulation output from OpticStudio:

$$R_{optics} = \frac{1}{\text{rmsRad} \cdot 2 \cdot 10^{-3}}. \tag{6}$$

For each of the above,the factor of 2 is due to the convention of using linepairs as a standard unit of measurement in optical systems, rather than just a single line. This allows the ability to eventually quantify not only system resolution, but also the transmission of contrast within a single parameter. The system resolution can then be calculated as per Auelmann's article via the General Image Quality Equation (GIQE) which utilizes an empirical exponent of -1.35 to account for system limitations and imperfections:

$$R_{system}^{-1.35} = R_{optics}^{-1.35} + R_{sensor}^{-1.35}. \tag{7}$$

We can use the value from Equation 7 to find what can be called an "effective pixel pitch," since it takes the place of the true pixel pitch in Equation 4 for GSD, but is now a larger value due to contributions from imperfect optical performance:

$$\text{Px}_{eff} = \frac{1}{R_{system} \cdot 2 \cdot 10^{-3}}. \tag{8}$$

We can then substitute these values into Equation 4 and obtain what can be called an "effective GSD," which is now much greater than the true (purely geometric) GSD:

$$\mathrm{GSD}_{eff} = \frac{\mathrm{Px}_{eff} \cdot 10^{-6} \cdot \mathrm{h} \cdot 10^{3}}{\mathrm{EFL}}. \tag{9}$$

From here, the system's effective resolution is twice the "effective GSD," or

$$\mathrm{Res}_{eff} = 2 \cdot \mathrm{GSD}_{eff}. \tag{10}$$

As discussed in later sections, this analysis matches experimental results when observing on-axis rays, but suffers as the angle of incidence increases. Thus, though it is a useful approximation for on-axis resolution prior to laboratory characterization, it is largely susceptible to variations in the RMS radius across the FOV, which varies significantly (even over short distances on the image plane) as one moves from the centre to the edge of the FOV. Usually, this is remedied using fully custom optics for consistent focus across the FOV, but for low-cost missions, a variance in focus across the FOV is a common concession. A more thorough discussion of resolution characterization in the laboratory is provided shortly.

Modulation Transfer Function

While resolution is a crucial benchmark in system performance, the Modulation Transfer Function (MTF) is equally important. A system's MTF characterizes the ability of a given system to transfer contrast at a particular resolution from the object plane to the image plane, effectively combining resolution and contrast into one parameter. Resolution is the system's ability to distinguish detail at a given frequency in lp/mm, whereas contrast is defined by how accurately the intensity maxima and minima are transferred from the object to the image plane. For a given line pair, as the spacing between decreases, the resolving power required to observe the two separate lines increases, and the ability for the system to transfer the contrast lessens, thus lowering the systems MTF value. Each component in an optical system has an associated MTF wherein the effects are multiplicative:

$$\mathrm{MTF}_{\mathrm{system}} = \mathrm{MTF}_{\mathrm{component\ 1}} \times ... \times \mathrm{MTF}_{\mathrm{component\ n}}. \tag{11}$$

According to Villafranca et al.,[10] the factors affecting the MTF most are those that arise from the optics, the detector, and the platform stability. Foremost, the optical MTF contribution is given by a plot obtained from Zemax OpticStudio. Next, detector MTF is given by:

$$\mathrm{MTF}_{\mathrm{detector}} = \left| \frac{\sin(\pi \cdot d \cdot f)}{\pi \cdot d \cdot f} \right| \tag{12}$$

where d is the size of the pixels, and by the definition of the Nyquist frequency, $\mathrm{f} = 1/2 \cdot d$. The platform stability contribution is calculated by:

$$\begin{aligned} \mathrm{MTF}_{\mathrm{platform\ stability}} &= \mathrm{MTF}_{\mathrm{linear\ motion}} \times \\ &\times \mathrm{MTF}_{\mathrm{jitter}} \times \mathrm{MTF}_{\mathrm{sinusoidal\ motion}}. \end{aligned} \tag{13}$$

Here, the linear motion contribution is given by:

$$\mathrm{MTF}_{\mathrm{linear\ motion}} = \left| \frac{\sin(\pi \cdot \alpha_{LM} \cdot f)}{\pi \cdot \alpha_{LM} \cdot f} \right| \tag{14}$$

where α_{LM} is the distance the target travels across the detector pixel in one integration time. If f is taken as $1/2 \cdot d$ and if α_{LM} is taken as d,[10] then we have $\mathrm{MTF}_{\mathrm{linear\ motion}} = \mathrm{MTF}_{\mathrm{detector}} = 0.64$.

Further, we have the jitter contribution:

$$\mathrm{MTF}_{\mathrm{jitter}} = \exp\left(-2 \cdot \pi \cdot \sigma^2 \cdot f^2\right) \tag{15}$$

where σ is the RMS displacement of the target at the detector. Finally, there is a contribution arising from the sinusoidal vibration of the spacecraft. However, both this contribution only arises to an appreciable degree for an imaging system with long integration times, and as such is omitted.[10] Further, it was reported that undesired jitter motion of less than 10% of a pixel causes negligible impact to the MTF; since our attitude determination and control system (ADCS) is reported to have stability of 0.003°/s, we find that the expected jitter motion for our spacecraft will translate to a minuscule portion of our ground sample distance.[10] It is noteworthy that there are also system MTF effects arising from Earth's atmosphere, but such effects are often small for aperture sizes under twenty centimeters in diameter.[16] As it relates to acceptable MTF for an imaging system, it has been previously reported that between 0.1 and 0.2 is fair for Earth-observation missions.[10]

Final VNIR Design

Figure 2 shows the flight model COTS VNIR design. In simulation, this design meets all mechanical and performance requirements, as it was a product of detailed work shown in the previous sections of this document. This design consists of three com-

mercial lens elements and one 45-degree folding mirror. We estimate the following average performance specifications for VNIR:

- Average resolution (400 km altitude): 192 m
- Average resolution (300 km altitude): 144 m
- Average MTF: 0.12

Here, we can see that even at the highest altitude (400 km), the average resolution (192 m) across the detector does not exceed the design requirement, which allows for imperfections such as thermal effects and manufacturing tolerances. Conservative estimates for thermal and tolerance effects suggest that the design will remain within requirements throughout mission life. Table 3 shows the diameters and effective focal lengths (EFLs) of the COTS lenses which comprise the VNIR system; note that they are numbered left-to-right and top-to-bottom, with incident light from Earth entering from the left.

Table 3: VNIR and SWIR lightpath optical element breakdown

Lens No.	Type	Diameter [mm]	EFL [mm]
1	Uncemented achromat	30	100
2	Negative meniscus	25.4	-1000
3	Positive meniscus	25.4	100

The MTF for the VNIR system is on the lower end of what Villafranca et al. report as fair (0.1 to 0.2), though it is still within the acceptable range.[10] Further, it is noted that the average MTF and average resolution calculations were done by taking into account the steepest (furthest FOV) rays as well as the direct rays, hence we anticipate targets near the centre of the FOV to show superior performance to these reported averages. In fact, the majority of the FOV is superior to the reported averages.

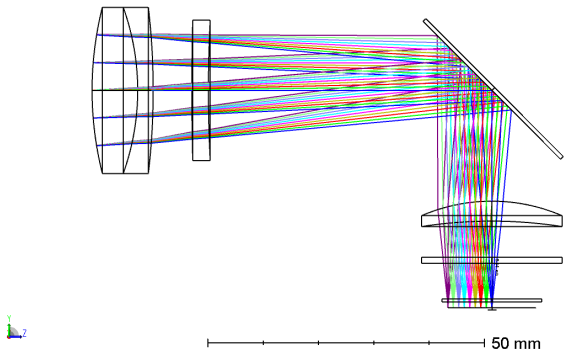

Figure 2: Visual-Near Infrared (VNIR) Optical Path

Final SWIR Design

Figure 3 shows the flight-model SWIR design. In simulation, this design meets all mechanical and performance requirements. As with the VNIR design, this design consists of three lens elements and one 45-degree folding mirror. We estimate the following performance specifications for SWIR:

- Average resolution (400 km altitude): 358 m
- Average resolution (300 km altitude): 269 m
- Average MTF: 0.20

The SWIR system consists of the same optical elements as the VNIR system shown in 3; though we see transmission losses in SWIR due to the use of common COTS glass (N-BK7 and N-SF5), we have taken these losses into account in our exposure analyses. For this design, we see similar performance margins as the VNIR design (i.e., over 100 m margin before exceeding the resolution requirement) with respect to absorbing thermal and tolerancing effects, and as such we expect the design to remain within performance requirements throughout the entire mission lifetime. For SWIR, the MTF for the SWIR system meets the upper end of what Villafranca et al. describe as fair (0.1 to 0.2).[10] Similar to VNIR, these the majority of the FOV has resolution and MTF values superior to the reported average due to steep decline at the edges.

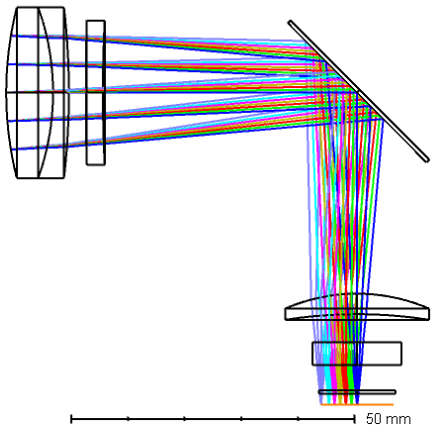

Figure 3: Short Wave Infrared (SWIR) Optical Path

Prototyping

In order to test our lens system with a fully functional electronics back-end prior to completion of the Iris electronics suite described later in this report, a Genie Nano 1 GigE G3-GM12-M2590 sensor was acquired. There are no significant differences between the Genie Nano and the CMV4000 sensor chosen for the Iris electronics save for pixel pitch (4.8 µm for our GigE Nano and 5.5 µm for the CMV4000) and in optimal spectral response. However, we can account for these differences within our calculations and simulations.

For testing, a positive USAF 1951 Test Target was acquired to aid in the characterization of the resolution performance of our lens system. An example test image using this target is shown in Figure 4. Using this target, we can analyze captured images and characterize the resolution of our system via external analysis by visual inspection, and eventually using custom code. The test target has a grid of groups and elements, with every pair of group and element corresponding to an intrinsic resolution in of:

$$R = 2^{G+\frac{E-1}{6}} \tag{16}$$

where G is the group number and E is the element number of the test target, and R is the resolution in linepairs per mm (lp/mm). Since the groups run from [-2,9], and elements [1,6], we have the ability to very thoroughly characterize our system resolution at a given distance from anywhere between 0.250 to 912.3 lp/mm. A disadvantage is that precise resolution characterization could be limited by the degree of granularity between steps in groups and elements.

Resolution Test Results

Due to the scarcity and high cost of InGaAs SWIR sensors, testing has only so far been performed on the VNIR subsystem using the Genie Nano 1, the stand-in sensor for the CMV4000 in testing. Once the Iris electronics back-end becomes more advanced and the Hamamatsu InGaAs G11478-512WB linear pixel array arrives, resolution will be characterized for the SWIR system in a similar manner to the process described below.

In the laboratory, the VNIR lens system was assembled and aligned utilizing an expanded laser focusing onto the Genie Nano 1. Images were then taken of the test target at varying distances, ranging from 2-10 m. A sample image is shown in Figure 4, which was taken at a distance of 4.66 m from the detector. These images were focused by hand, and multiple images were taken at each distance over varying fields of the focal plane (directly on-axis, halfway across FOV, and then at the edge of FOV), allowing for the characterization of the resolution performance across the entirety of the image plane. These images were then inspected for resolvable group and element on the test target.

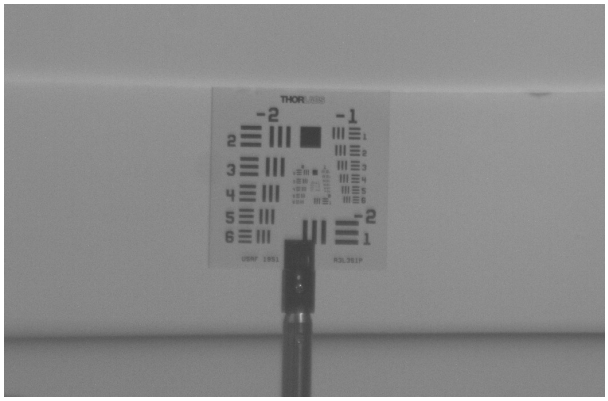

Figure 4: Sample image of the test target taken from a distance of 4.66 m

Note that the figure above has been cropped to adequately show the USAF 1951 Test Target, placed at the center of the field of view. Results from one particular experiment are shown in Table 4, though this is just one subset of multiple characterization experiments performed (and yet to be performed). In Table 4, R_{exp} is the expected resolution in meters at an orbital height of 400 km, and R_{sim} is the resolution at 400 km obtained from the simulation analysis method described above.

Table 4: Example resolution estimates based on resolution experiment

Position	Distance [m]	R_{exp} [m]($\pm \sim 10$)	R_{sim}[m]
On-axis	4.66	85.8	78.3
	5.81	86.7	
	7.87	80.7	
Mid-FOV	4.66	96.4	86.8
	5.81	122.7	
	7.87	143.8	
Far-FOV	4.66	192.7	248
	5.81	194.7	
	7.87	161.4	

That is, R_{exp} is the actual resolution we might expect in orbit with the system under test, while R_{sim} values are based the resolution estimation method described above in this report, which utilize simulation outputs from OpticStudio. The experimental values have an error of about 10 m, as each successive element in a given group on the test target increases or decreases in line-size by approximately this amount.

Results from in-lab experiments closely match the expected resolution only when the target is on or near the center of the image ("on-axis"), but then overshooting or undershooting resolution in simulation compared to experiment for the mid- and the far-FOV results. This is likely due to significant variance in RMS spot radius as a function of FOV at mid-FOV and further. In reviewing OpticStudio simulation outputs, a far steeper rate of change in RMS spot radius occurs past the mid-FOV than nearer to the centre.

Further, it is easier to be precise in estimating the correct RMS radius to choose for comparison for an on-axis image versus a mid-axis image, since we are required to subjectively place the test target at some point at mid-FOV, which corresponds to a given RMS radius with minimal margin for error. It is possible to get a fair estimate for resolution at mid-FOV, but it largely depends on ability to fortuitously pair the correct mid-FOV RMS spot radius with placement of the target in the image. These challenges are in addition to imprecision introduced by the step-sizes for resolved groups and elements on the target itself. As such, we suggest our model for estimated performance is useful primarily for on-axis light, and for the wider FOV imagery, laboratory characterization of system resolution is essential.

Analysis Code

Another challenge inherent in this method is the subjectivity of human observers in determining a "resolved" group and element pair on the test target. Thus, code is being developed in-house to aid in the characterization of system resolution by minimizing opportunity for error in subjective interpretation of resolution. Note that the analysis above was done without the code, and the code is being designed for future characterization of flight designs.

For a given image, the code will prompt the user to select any group and element pair that the user deems to be "resolved." The code will then integrate each pixel column for an effective lineout and normalize the data. A plot of normalized pixel value versus column number would be a Heaviside function in an ideal case, however, due to MTF losses and a finite pixel size, we do not see a sharp change in contrast between two adjacent lines. Ergo, we observe a gradient between the two lines with a Gaussian-shaped peaks, and fit an Gaussian to it. We can then obtain the full-width at half-maximum (FWHM) for this fit, which gives us a value of the width in pixels of one line in an image. Since we know the distance at which the target was placed for a given image, we can then calculate our empirical resolution.

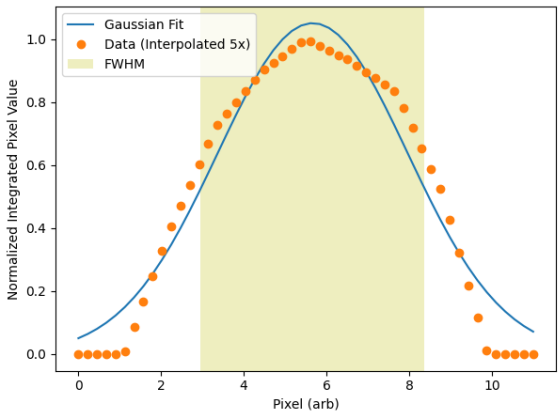

Figure 5: Sample plot obtained from analysis code of group -2, element 3 from the test target, in an image taken at a distance of 4.66 m from the detector.

After obtaining a number of these plots from a specific group and element on the test target, we can take the mean FWHM value and convert it into a length measurement. The ability to back-solve for the expected group and element pair stands to

confirm or refute subjective interpretation of resolution. For a given image, when the code correctly relays back to the user the selected group and element, then that group and element is considered "resolved" at that distance. This helps eliminate human bias or interpolation error which could arise due to a human's prior knowledge of what is being viewed on the target. This code ultimately seeks to streamline analysis workflow and remove as much subjective analysis as possible. Initial results are promising and full useful functionality is expected to be achieved over the course of Summer 2021.

MECHANICAL

Structure Design Overview

Similar to the optical design, Iris' mechanical structure is designed by the AlbertaSat student team. The purpose of the Iris structure is to house Iris' optical elements within their required tolerances and securely mount Iris to Ex-Alta 2's CubeSat frame. Figure 6 shows the main components which make up the Iris structure. As previously mentioned, the Iris payload has two optical paths: one for imaging around the 2100 nm band (SWIR) and one for imaging around the 865, 490 and 665 nm bands (VNIR). The optical path of both SWIR and VNIR optics are separated by a 45° folding mirror to reorient the light path 90°. This allows for a longer light path to fit within the Iris maximum volume budget of 1U.

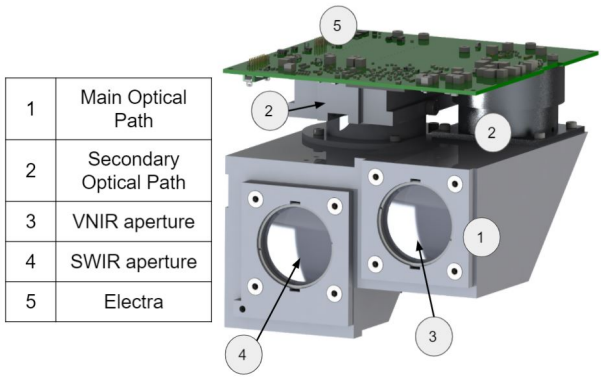

Figure 6: Render of Iris payload with main structural components annotated.

Structure Material Selection

Material considerations for the Iris structure are density, strength-to-weight ratio, machinability, thermal conductivity, thermal expansion characteristics, and ferromagnetic properties. To comply with Ex-Alta 2 system requirements, Iris is required to be remain under 1.3 kg. Iris' mass can be minimized by selecting a material with low density and high strength-to-weight ratio. Materials with long lead times and complex machining techniques increase the barrier for students to machine the structure themselves, and so machinabilitiy of the material is of high priority. Thermal conductivity is considered in the material selection, because highly thermally conductive material can dissipate the heat created by the Electra printed circuit board (discussed below) as a means of passive thermal control. Selecting a material with a low thermal coefficient of expansion reduces the amount of movement the optical elements experience over the Iris operational temperature range. Furthermore, materials with small pockets of air, such as 3D printed materials, are not suitable for the vacuum of space. Employing these material selection guidelines, Aluminum 6061 T6 was chosen as the material in the Iris structure due to its high thermal conductivity, high strength to weight ratio, relatively low density, low ferromagnetic properties, and ease of machining.[17]

The Iris structure follows the following structural design guidelines to facilitate an easy assembly, decrease machining costs, and increase structural stability:

- All fasteners should be secured into threaded holes instead of using nuts. This reduces the part count of the system and simplifies the assembly process. Nuts are hard to hold in place and hard to fasten with appropriate torque, especially in small compact assemblies. Wherever possible, blind holes are to be avoided. This will prevent small pockets of air becoming trapped within the threads.
- Aluminum 6061 T6, when compared to the stainless steel fasteners, is soft. To increase the strength of the threads, Helicoil inserts should be installed into the threaded holes.
- When possible, commercial-off-the-shelf (COTS) components are used for optical and mirror mounting, in attempts to minimize cost and design complexity.
- Iris' design is developed with ease of assembly and harnessing in mind.

Table 5 shows a mass breakdown of Iris' components. The aluminum structure includes the main and secondary optical path bodies, and the optical

mounting structure include the lens and mirror holders. The optical elements refer to the lens and mirror. Furthermore, the optical mounting hardware includes springs, spacers, shims, and threaded retaining rings. Threaded fasteners include the socket head and flat head screws used, in addition to the Helicoils. See Figure 7 for an exploded view of the Iris structure showing the different components.

Table 5: Iris mass breakdown - current best estimate

Iris Subsystem	**Mass [g]**	**Percent Of Mass Requirement % (1.33 kg)**
Aluminum 6061-T6 structure	687.15	51.67%
Optical elements	59.44	4.47%
Optical mounting structure	91.03	6.84%
Optical mounting hardware	36.25	2.73%
Threaded fasteners	29.92	2.25%
Electra PCB	28.14	2.12%
Total	**931.93**	**70.07%**

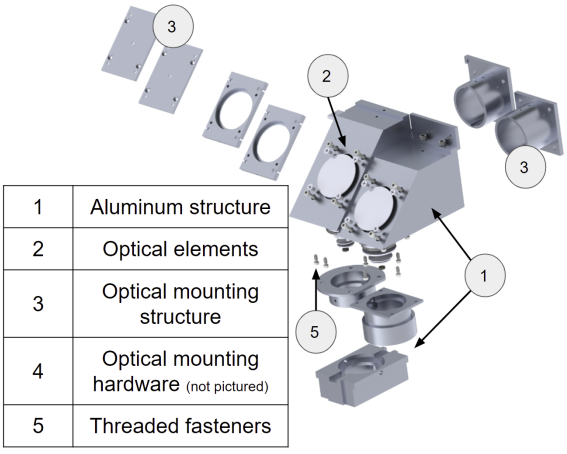

Figure 7: Exploded view of Iris showing the components classified in the mass breakdown.

Lightpath alignment

Iris' structure is required to align the focused image plane directly onto the photosenstive area of the both sensors. To reduce part count and increase the precision of alignment between the VNIR and SWIR optical paths, the main optical path is fabricated from a single piece of aluminum, as shown in Figure 6. The main optical path houses the primary set of lenses and defines the position of each aperture, as shown in Figure 6. The secondary optical paths are fastened to tapped holes in the main optical path using four screws for each optical path.

The period in which Iris will experience the largest acceleration is during the rocket launch. Therefore, all aspects of the Iris structure are designed to maintain structural integrity during the launch environment, specified by the NanoRacks CubeSat Deployer Interface Definition Document.[18] One interface that requires strict alignment is between the Electra printed circuit board and the secondary optical path. This interface aligns the photosensitive areas with the incoming focused light. To ensure proper alignment after the vibration experienced during launch, each secondary optical path is rigidly mounted to Electra with four threaded fasteners. Finite element analysis (FEA) was conducted on the Electra/secondary optical path interface, and it was found that Electra does not experience significant stress due to the vibration of the Iris structure. The VNIR secondary optical path is mounted directly in the centre of the lightpath hole in the primary optical path, and the centre of the photosensitive area of the VNIR sensor on printed circuit board.

Optical element mounting

In compact optical designs like Iris, the positional tolerance of the optical elements is very tight. The structure could simply be machined within these tolerances to obtain the required placement however this method increases machining costs and leaves little room for quick and cheap post-assembly adjustments. Due to the team's inexperience with designing and assembling optical systems, it is expected Iris' optical elements will benefit from some form of post-assembly adjustment to obtain complaint image quality. The design of Iris' structure allows for easy access to these adjustment areas. Manual adjustment mechanisms, which allow for fine-tuned adjustment of the mirror plane orientation and axial position of the lenses are integrated into the Iris structure. Both lens and mirror adjustment mechanisms are described in detail in the following subsections.

Lens mounting

Lens mounting in the primary and secondary optical paths share a similar design. Axial adjustments of the lenses is accomplished by positioning the lenses between a wave spring and a threaded retaining ring, that engages with internal threads in

the lens holder. The lenses must be preloaded so they remain static during launch but not to a point where risk of deformation or fracture is introduced. This preloading balance must hold true over the entire allocated axial adjustment range of the wave spring. This dictates the spring constant and work height of the selected wave springs. The axial adjustment range of the lenses is +/- 0.5 mm, but can be modified if it is determined during functional testing that a larger post-assembly adjustment range is required.

The use of retaining rings to secure the lens allows for quick assembly and disassembly and controlled axial adjustments, whereas other methods, such as snap rings, press retainers and elastomers, do not. To ensure proper distance of the two lenses within the baffle of the main optical path, a spacer is placed between them. The tolerance of the length of the spacer is made as tight as possible, however unlike the other parts of Iris, the optical spacers are simple enough to be accurately manufactured by student machinists. The spring force is evenly distributed over the entire free aperture of the lens with a shim that sits between the wave spring and the lens. The inner diameter of the threaded retaining ring, shim, and spacers are identical, which prevents any internal bending moment within the optical mounting hardware.

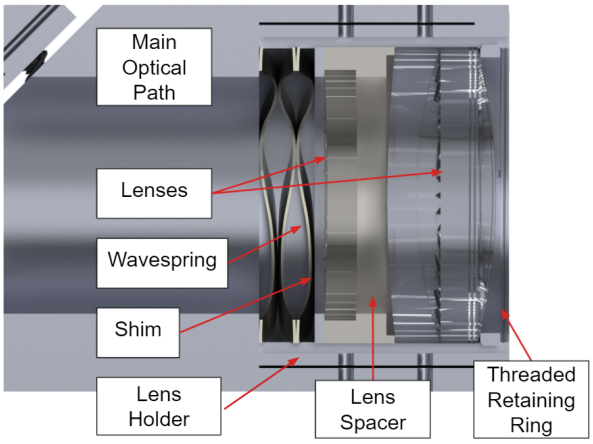

Figure 8: Cross section of the SWIR primary optical path, showing the lens mounting and adjustment system.

The inner diameter of the lens holders are each machined 25 to 50 µm larger than the diameter of the lens to allow for easy loading into the assembly.[19] As the threaded retaining ring preloads the lenses against the wave spring, it will center the spherical lens about its free aperture. The inner diameter in the main optical path which houses the wave spring is toleranced tightly, to ensure proper alignment of the lens about the main optical path. The wave spring will be able to withstand the compressive hoop stress at lower temperature. Once the lenses and spacers are inserted into the lens holder and fine adjustments are made to the position of the optical elements, the lenses are potted in place with RTV566 silicone rubber compound. RTV556 has space heritage in similar applications and provides low outgassing characteristics in a high vacuum environment.[20] The compound is injected through concentric holes travelling through the main optical path and lens holders. The epoxy will travel through these holes and through grooves which run along the length of the lens holder's inner diameter, as shown in Figure 9. The grooves will allow the epoxy to travel to the outer diameter of the lenses and spacers which make up the lens set. Functional testing is required to ensure that the potting compound travels through the entire length of the groove without epoxy bleeding into the clear apertures of the lens. All epoxy used will be vacuum cured to prevent trapping any small pockets of air.

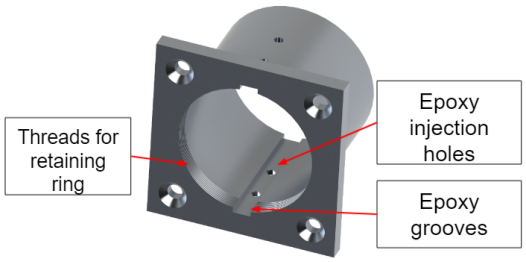

Figure 9: Render of the lens holder, showing the epoxy holes and grooves.

Lens Stresses

Two primary stresses act on the lenses: one being hoop stress inflicted on the lenses by temperature changes within the structure, another being axial stress on the lenses due to preloading inflicted by the wave spring.

As the Iris structure expands, both the RTV556 epoxy and wave spring preloading will keep the lens in place. The diameter of the lens barrel will be machined just large enough so the lenses do not experience any hoop stress as Iris drops to its minimum operational temperature of -30 ℃. As mentioned previously, the inner diameter of the lens holder should be

at least 25 to 50 µm larger than the outer diameter of the lens to ease assembly. The initial nominal inner diameter of the lens holder is chosen within this range. The amount the inner diameter of the lens holder contracts can be calculated with the following 2D thermal contraction calculation:

$$\Delta A = A2\alpha\Delta T \tag{17}$$

where ΔA is the change in area in mm^2, A is the initial area of lens barrel cross section in mm^2, α is the thermal coefficient of expansion in $°C^{-1}$, and ΔT is the change in temperature in °C. The final dimensions of the lens holder inner diameters are specified to ensure that the change in the inner diameter of the lens holder due to a decrease in temperature will not interfere with the outer diameter of the lens over Iris's entire temperature range. As the lens holder contracts, the cured epoxy will press into the lenses, however it is not expected to cause any deformation in the lenses.

The lens will experience axial stress around about the perimeter of its free aperture due to wave spring preloading. The lens will stay rigid during launch (99.7 % confidence interval) if the wave spring preload force exceeds the 17.28 g or 174.6 m/s^2.[18] Note that the potting epoxy will be used to further secure the lenses. In the worst case, the g-force would be applied in the opposite direction to the preload supplied by the wave spring, creating zero net force on the lens in the axial direction. This is the condition in which the preload of the lenses is calculated. The preloading force required to keep the lens in place during maximum acceleration is calculated as

$$F_{preload} = m_{lens} \cdot a_{launch} \tag{18}$$

where $F_{preload}$ is the wave spring preloading force required and m_{lens} is the mass of the lens(es) held by a wave spring.

The preloading inflicted by the wave spring should not exceed this calculated value by any significant amount to prevent deformation of the lens. A rule-of-thumb tensile design strengths for nominal glass materials is 1000 - 1500 psi.[21] Each lens set has a mass on the order of 50 g, which makes the required preload to maintain rigidity relatively small. Therefore, there is no concern of the retaining ring inflicting a tensile stress of enough magnitude to damage the lens.

Optical Bonding Epoxy

For added contingency, the amount of epoxy bonding surface area between the lenses and lens holder is designed to be sufficient to hold the lenses in place without any preloading provided by the wave spring and threaded retaining ring. The minimum bond area of the epoxy is calculated and the epoxy grooves are designed to exceed the minimum bond area. Since the lenses sit within the lens holder's inner diameter, they can only shift axially or rotate. Therefore, the bonding epoxy can only yield through shearing. RTV566's shear strength, G, is 22.06 MPa.[20] The shear stress experienced at a bond is calculated with the following equation:

$$G_Y = Ma/A^{22} \tag{19}$$

where G_Y is the shear strength in MPa, M is the mass of the lens element in kg, A is the bond area in m^2, a is the acceleration experienced in m/s^2. Using the maximum acceleration value Iris will experience during launch of 174.6 m/s^2 and the shear stress of the RTV566 compound, the equation above can be used to find the minimum bond area to ensure the epoxy does not yield.[18] The minimum bond area required to hold a 50 g lens element is 0.4 mm^2. 50 g is an appropriate order of magnitude estimate for the final mass of one lens set. This optical bond surface area is well accounted for if the epoxy is distributed along two grooves currently designed into the lens holder. This process is used to verify the groove dimensions exceed the minimum bonding surface area required to bond each lens set.

Mirror Mounting

Like the lenses, it is advantageous to design the mirror mounts such that their alignment can be adjusted post assembly. This section will outline the mirror mount adjustment mechanism. Both SWIR and VNIR mirror mounts are similar in design, with slightly different dimensions.

The 45-degree folding mirrors which re-orientates Iris' lightpath sit in mirror mounts separate from the main optical path structure. Figure 11 shows the anatomy of the mirror mount sub-assembly. Like the main optical path, Aluminum 6061 T6 is selected for the mirror mount material. The mirrors sit inside a framed mirror lens holder, and the cover plate secures the placement of the mirror from the back. Six pieces of *Viton* cord stock are placed around the perimeter of the mirror between the back of the mirror and cover plate to gently preload against the mirror holder, which will absorb vibrations it will

experience during launch. Four threaded fasteners which interface the mirror mounts with the main optical path double as the mirror mount adjustment mechanism.

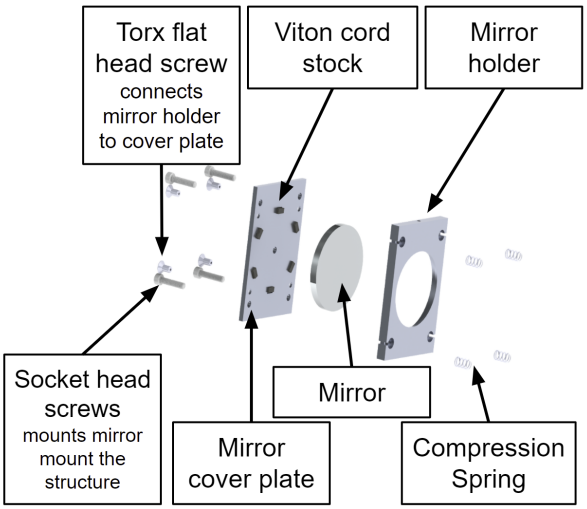

Figure 10: Exploded view of the mirror mount assembly.

The fasteners sit inside compression springs, whose ends press up against the mirror mount and main optical path, shown in Figure 11. The height of each of the four corners of the mirror mount can be adjusted by engaging and disengaging the fasteners, which provides the post-adjustment alignment capability. As a result, when the fastener is tightened, the spring is compressed and provides an upward compression preloading force, keeping the mirror pressed up against the threaded fasteners as its alignment is adjusted. Much like the wave springs used to axially adjust the lenses, the compression springs used in the mirror mount sub assembly are specified to provide the necessary preload to keep the mirror in place during rocket launch, while minimizing bending stress within the mirror mount.

The mirror mount has the ability to modify the mirror plane by $\pm$ 3.96° in any direction before the fastener interferes with the inside diameter of the screw holes. However, an adjustment range of $\pm$ 1° from the nominal mirror position has been chosen as it is expected that post-assembly alignment will not require a larger range.

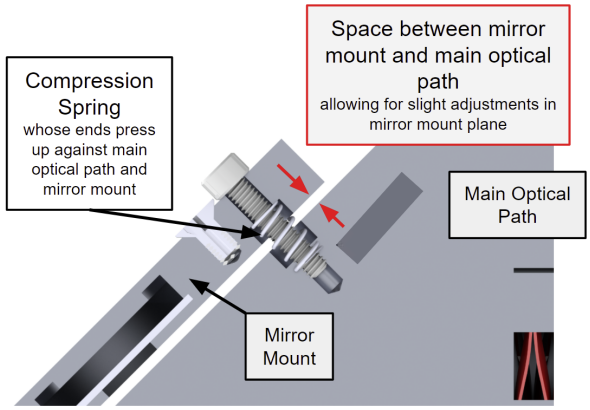

Figure 11: A cross section of the mirror mount design, showing the small adjustment space between the mirror mount and main optical path.

Similarly to the wave springs in the lens mounts, the compression springs which preload the mirror mount are specified to provide a sufficient preloading to keep the mirror mounts in place during launch without the aid of epoxy. After the post-assembly adjustment is completed, the fasteners will be epoxied to both the mirror mount and main optical path as a secondary locking feature.

Rotating one of the mirror mount fasteners by 10 degrees (0.175 radians) translates to an vertical displacement of 13.9 µm at the corner of the mirror mount. This adjustment resolution is determined to be sufficient to provide fine-tune adjustments to the mirror plane. However, if the adjustment resolution is found to be too coarse during functional testing, screws with a finer pitch will be used for this interface.

ELECTRONICS

A custom printed-circuit board (PCB) called Electra houses the image sensors, control circuitry, memory, and power regulators for Iris' orbital imaging operations. As with most of AlbertaSat designs, this PCB was designed in-house, and has had versions prototyped using both in-house and outsourced assembly. In particular, the device features an Intel System-on-Chip Field Programmable Gate Array (SoC FPGA) integrated along with one CMOS area scan imager for VNIR imaging and one InGaAs linear array for SWIR imaging. The selection and integration of these components is discussed below, along with other critical details of Electra's design.

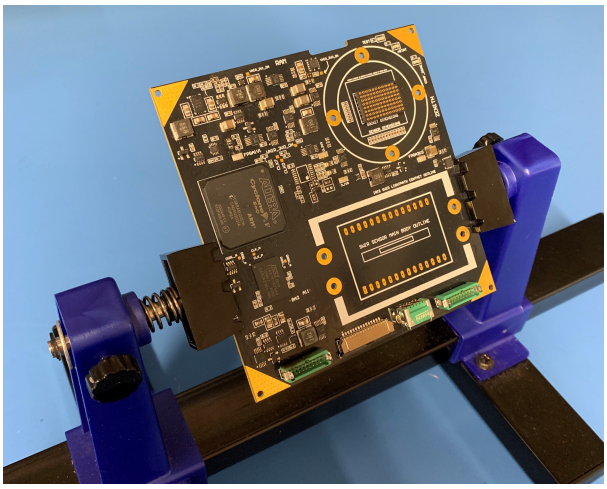

Figure 12: Prototype Electra PCB during preliminary functional testing.

SoC FPGA Selection

We chose an FPGA with embedded dual-core ARM processor ("system-on-chip") to manage image sensors including timing generation, image capture, control of multiple interfaces, and communication with the on-board computer (OBC). The selection of an FPGA system-on-chip (SoC) is motivated also by AlbertaSat's guiding ethos of lowering the barrier of entry to space as it develops open-source hardware and firmware, since Electra offers significant computational ability for any future missions that do not have a dedicated OBC. The relationship between the OBC and Electra for the Ex-Alta 2 mission is described in sections below.

In addition to traditional space mission requirements for components which relate to off-gassing, temperature, and other characteristics, the characteristics of interest with respect to selecting an SoC FPGA were:

- The ability to write image data to SDRAM at speeds up to 480 Mbps,
- Have at least 19 low-voltage differential signalling (LVDS) channels for VNIR image data, and
- Have at least 1 GB of addressable random access memory (RAM).

The Cyclone V device family from Intel was chosen because it met each of the above criteria and development hardware was available to the team early in firmware design stages. The exact device chosen is the 5CSEBA6U23I7N, which features a dual ARM Cortex-A9 processor in addition to its FPGA logic elements. This device is large with 672 pins, but it is required in order to accommodate the differential signalling pairs for our chosen sensor, which is discussed below.

Sensor Selection

VNIR Sensor

As discussed, Iris uses pushbroom imaging to capture two-dimensional images using linear arrays (or individual rows of area arrays acting as such). The CMV4000 CMOS area sensor from *ams* was selected as the VNIR image sensor. In addition to suitable spectral parameters, this device was chosen due to its windowing capability, meaning our subsystem VHDL can select particular pixel rows from the pixel array individually and store them separately. Hence, by placing a multi-zone filter over this sensor, we can individually read out images in multiple bands using one sensor as the spacecraft sweeps the ground area, as discussed later in this report.

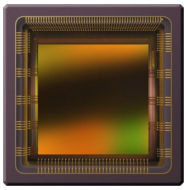

Figure 13: CMV4000 CMOS image sensor chosen for integration onto Electra.

Further, in order to reduce risk of loss of sensor for PCB prototype iterations, a ball-grid array (BGA) socket was implemented on the PCB for straightforward application and removal of the sensor, which is a pin-grid array (PGA). This sensor also features small pixel pitch (5.5 µm) for adequate spatial resolution performance.

SWIR Sensor

The chosen sensor for SWIR reflectance data is the G11478-512WB linear pixel array from *Hamamatsu*. This device only features one linear array of pixels, meaning it will be operated in a simple linescanning fashion as the spacecraft sweeps the ground area. This particular sensor was chosen due to strong spectral response in our SWIR band of interest, moderate noise, and the opportunity to operate a built-in thermoelectric cooler. The 512-pixel

variant was chosen due to smaller pixel size for increased spatial resolution.

Figure 14: G11478-512WB InGaAs linear array chosen for integration onto Electra.

Design Overview - Hardware

A simplified block diagram of the Iris electronics is shown in Figure 15, which shows the main components of the imaging electronics system: The hard processor core, the FPGA, the image sensors, onboard synchronous dynamic RAM (SDRAM), and the spacecraft OBC. Additionally, the electronic power system (EPS) is shown attached to the Controller Area Network (CAN) bus. This section will elaborate upon details of the PCB hardware implementation, design choices, and key features which make Iris a compact, modular payload suitable for future missions. Further, it will describe the nominal operation of the device in orbit as planned for the upcoming Ex-Alta 2 mission.

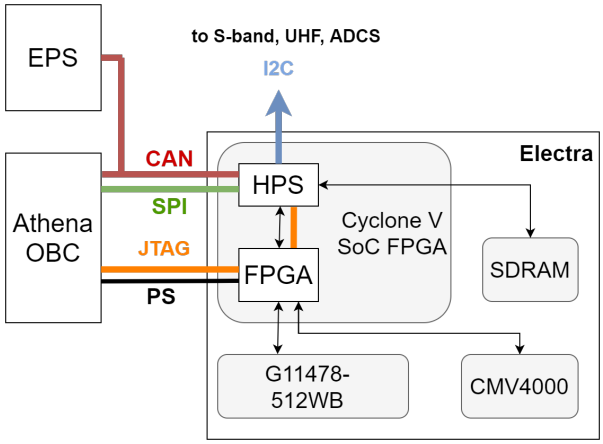

Figure 15: Simplified block diagram of Electra.

Interfaces

Electra has multiple hardware interfaces:

- CAN bus infrastructure for the receiving of commands from the OBC, and for transmitting watchdog signals to the OBC.
- Serial Peripheral Interface (SPI) for the delivering of image data to the OBC.
- I2C for in-orbit failure mode recovery if the OBC reaches an unresponsive state.
- Wires for the passive serial (PS) FPGA configuration scheme (see below).
- JTAG connection for assembly, integration, and testing (AI&T) prior to flight.

The inclusion of all of these hardware interfaces increases Iris' portability to future spacecraft missions.

Nominal Operation

Electra will be turned off when not in use, and turned on and re-programmed shortly ahead of an imaging sequence. A later section describes the methodology by which the OBC will configure Electra. In the meantime, each time the OBC powers up Electra, the following general steps occur:

1. The OBC programs the FPGA on Electra over point-to-point wiring, which contains the software image for the hard processor. The hard processor then boots from the FPGA fabric.
2. The OBC may now send commands to the software running on the hard processor via the CAN bus, which could include a command to take an image. The software passes all relevant data and commands to the FPGA virtual hardware description language (VHDL) within on-chip bus architecture. If the data is an image command, the VHDL will carry out its logic to gather spectral data using the image sensors and pass the data to the DDR3 SDRAM device on Electra.
3. When requested to retrieve and deliver the image from the OBC over CAN bus, the hard processor can access the SDRAM and deliver the image to the OBC over SPI for storage on the OBC SD card.

Single-event Latch-up Protection

One concern for space missions are the risk of high-energy particles causing single event CMOS latch-up, wherein nominal operation of a device is interrupted and high current draw can ensue. This can damage or destroy electronic devices. Electra features a thorough latch-up protection scheme wherein each power domain has a current sense resistor and an INA226 current sensing integrated circuit (IC) in

series with the supply, as shown in the example in Figure 16.

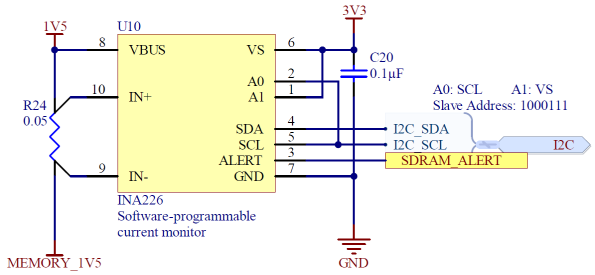

Figure 16: Current sense scheme for one of the device power supplies. There are ten such instances of this design on Electra for ten different power domains.

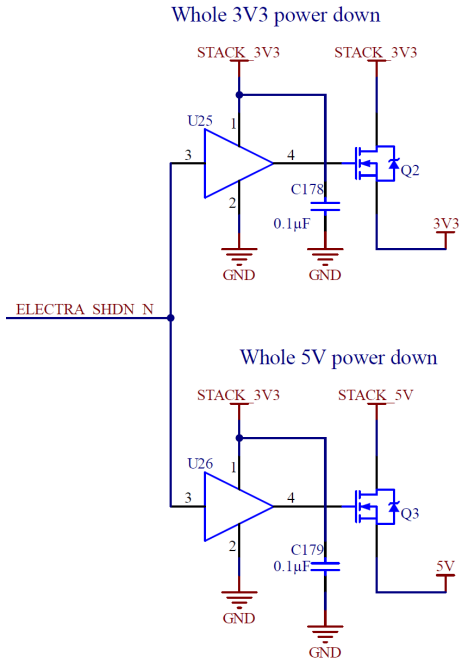

Figure 17: Full Electra shutdown scheme upon sensing of over-current by any one of ten INA226 current sensing ICs.

If the programmed current limit is exceed on any one INA226 sensors, another IC is implemented to cut power to the entire board for about ten seconds by the circuit shown in Figure 17, thus clearing the latch-up condition. After the timer is complete, the shutdown wire is released high, at which time power is restored to the board. In addition, and as another layer of redundancy, a watchdog timer is to be sent to the Electrical Power System (EPS) which will shut down power to Electra if a signal is not received over some programmable delay. Both of these implementations protect Electra from single-event latch-up by means of hard reset, with the on-board implementation supporting the use of Electra as a stand-alone OBC for future missions.

Programming Methodology

As discussed, the OBC will program Electra via a straightforward method called passive serial configuration, which is shown in Figure 18. On the programming micro-controller, we have selected general purpose input/output (GPIO) pins as well as leftover dedicated SPI pins for this programming scheme, wherein configuration data is simply clocked over the DATA0 line (with an associated clock, DCLK) after asserting nCONFIG to start the process. The primary benefit of this selected scheme is its simplicity as well as the ability to clock in configuration data at any desired speed whatsoever.

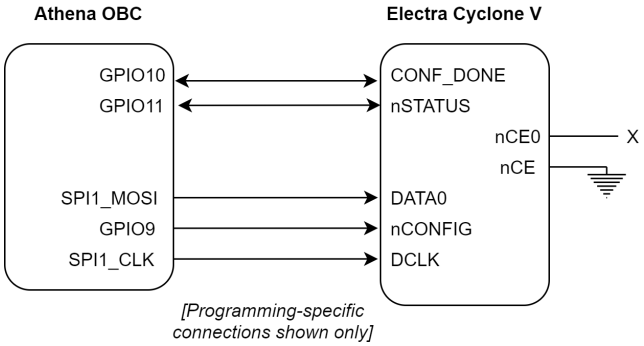

Figure 18: Passive serial configuration scheme between the OBC and Electra.

The Electra firmware image which will run on the hard processor will be included in the FPGA configuration data, along with the preloader. The hard processor will boot from the FPGA and run its bare metal application out of FPGA RAM or external SDRAM. This frees up component space on Electra, and eliminates the need for the OBC to access some external flash device or SD card to load in a new Electra software image in addition to the existing wires.

Design Overview - Firmware

Electra will feature an Intel SoC FPGA, DDR3 SDRAM, and two image sensors. In addition to the custom PCB design required to support this payload, a custom design is required in virtual hardware description language (VHDL) and software in

order to support image readout upon command and the subsequent transfer of image data to the OBC for downlink. This section will briefly describe the overall system design as well as Iris' pixel readout mechanism.

System Description

A simplified software and VHDL system block diagram is shown in Figure 19. The overall design features five distinct subsystems which handle specific functions on-board Electra. These are described in an enumerated list below.

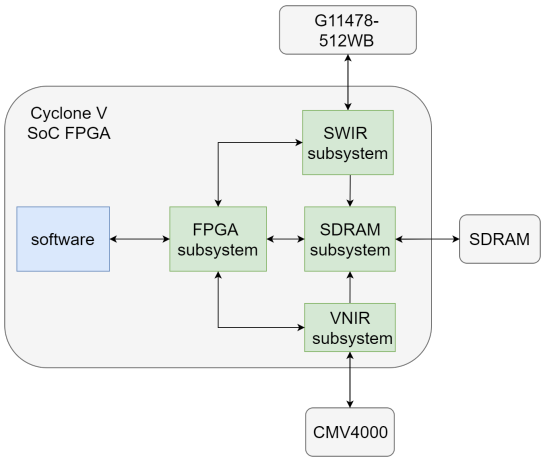

Figure 19: Simplified Electra firmware system block diagram. Green blocks are VHDL, blue blocks are software, and grey blocks are hardware components.

With the exception of the image readout methodology described in the next section, low-level details of the software and VHDL implementation are omitted for this report:

1. **Software:** This is software (written in C) which serves as the OBC's main interface to Iris. The software handles and passes commands to the VHDL subsystems, retrieves images from SDRAM when requested, and can apply compression algorithms to the retrieved data. The software also sends a watchdog signal to the EPS for additional single-event latch-up protection.

2. **FPGA Subsystem:** This subsystem is the primary interface between the software (running on the dual-core ARM processor) and the VHDL subsystems (which are configured in the FPGA fabric). It passes configuration data and commands to the lower-level subsystems, and applies any necessary type or data conversions.

3. **VNIR Subsystem:** This subsystem provides the interface for interacting with the CMV4000 image sensor, and is the source of all logic and timing for proper image readout. Data from this subsystem is passed to the SDRAM subsystem for storage.

4. **SWIR Subsystem:** This subsystem performs a nearly identical function to the VNIR subsystem, but for the SWIR sensor. This subsystem is only required to read out one line of pixels per integration time since the chosen detector is a simple linear array, however, it must also simultaneously control an external analog-to-digital converter (ADC).

5. **SDRAM Subsystem:** This subsystem is responsible for writing the data from the VNIR and SWIR subsystems to DDR3 SDRAM on Electra and ensuring the software has access to the address information of these images.

Image Readout

Both the VNIR and SWIR detectors gather spectral data using pushbroom imaging techniques. As shown in Figure 20, a linear array of pixels is used to gather the across-track dimension of image, which is integrated over multiple ground areas as the satellite carries out its orbit in order to acquire the second dimension of the photo.

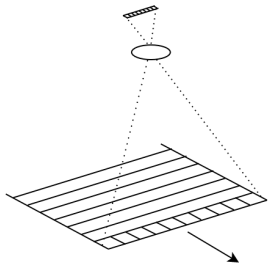

Figure 20: Pushbroom imaging using linear array of pixels (not to scale).[?]

Since the chosen SWIR detector is a simple linear array, the pushbroom methodology may be applied in a straightforward way. Regarding the VNIR detector, as mentioned above, a custom multizone filter is required in order to achieve three-band readout of a given ground area. A conceptual drawing of the filter overlay is shown in Figure 21.

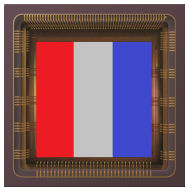

Figure 21: Conceptual drawing of filter overtop CMV4000 sensor photosensitive area.

Electra's VHDL controls different "windows" of pixel rows separately, ensuring that while each image in a given color will start at a different time, the images will correspond to the same ground area. This is illustrated in Figure 22, where one ground sample can be imaged by multiple rows of the same band, and then combined and averaged for increased SNR. Note that the number of rows per band and the number of rows separating bands is not to scale.

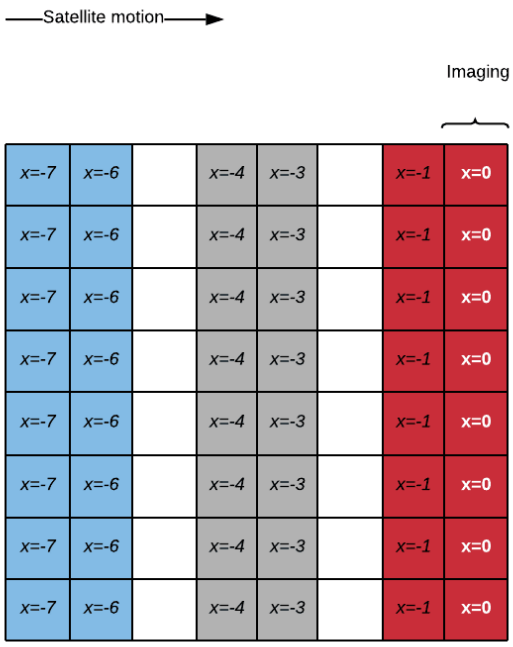

Figure 22: Illustration of Electra VNIR band readout methodology.

By this filtering methodology, the CMV4000 can be operated as three separate sensors, each reading out lines of pixels in one of three colors using the pushbroom method. This was used to replace a previous design which featured three independent linear array detectors.

CONCLUSIONS AND FUTURE WORK

This report describes advanced design details concerning a compact multispectral imaging payload for CubeSats called Iris. Optical performance specifications for the imager were presented along with detailed descriptions of exposure and resolution analyses which aid as a starting point for future teams to design and characterize an imaging system; of note is the use of strictly commercial-off-the-shelf optical elements as opposed to fully custom elements in order to significantly drive down cost. Additionally, the mechanical design of Iris, including main body design, lens fastening, mirror mounting, and other interface details were discussed. Electra, the imaging PCB for Iris, was described with a high-level overview of its components, nominal operation and image readout, PCB design, and firmware design.

A prototype of Iris is well underway and is expected to advance significantly over Summer 2021. Physical prototypes of the lens and mirror mounting designs have been assembled; and testing using the flight-ready optical elements is expected to occur in June of 2021. As of the end of May 2021, the Electra custom PCB has been demonstrated to be programmable using Passive Serial and JTAG configuration, with SDRAM and imaging experiments to begin in June of 2021. By August of 2021, a full VNIR imaging demonstration using flight-iteration electronics, optics, and structural design is expected. Full SWIR imaging demonstration is planned for early Fall of 2021. A proto-flight model will be integrated as part of Ex-Alta 2 proto-flight "flatsat" system testing by early December 2021, with delivery of the Iris flight model to the Ex-Alta 2 assembly team by December 24, 2021.

ACKNOWLEDGEMENTS

This project has been undertaken with support from the Canadian Space Agency, NSERC, the University of Alberta, the University of Alberta Faculties of Engineering and Science, CMC Microsystems, and individual donors. We would like to thank the many participants on the AlbertaSat team who provided outstanding design work and assistance, as well as those at Wyvern who provided frequent optical analysis guidance.

References

[1] Nasir Saeed, Ahmed Elzanaty, Heba Almorad, Hayssam Dahrouj, Tareq Y. Al-Naffouri, and Mohamed Slim Alouini. CubeSat Communications: Recent Advances and Future Challenges. *IEEE Communications Surveys and Tutorials*, 22(3):1839–1862, 2020.

[2] Nicholas Sorensen. Ex-alta 2 flight configuration render, 2021.

[3] Zhangyan Jiang, Alfredo R. Huete, Jin Chen, Yunhao Chen, Jing Li, Guangjian Yan, and Xiaoyu Zhang. Analysis of NDVI and scaled difference vegetation index retrievals of vegetation fraction. *Remote Sensing of Environment*, 101(3):366–378, 2006.

[4] Compton J. Tucker and Bhaskar J. Choudhury. Satellite remote sensing of drought conditions. *Remote Sensing of Environment*, 23(2):243–251, 1987.

[5] Arnon Karnieli, Nurit Agam, Rachel T. Pinker, Martha Anderson, Marc L. Imhoff, Garik G. Gutman, Natalya Panov, and Alexander Goldberg. Use of NDVI and land surface temperature for drought assessment: Merits and limitations. *Journal of Climate*, 23(3):618–633, 2010.

[6] A.R Huete. A soil-adjusted vegetation index (savi). *Remote Sensing of Environment*, 25(3):295–309, 1988.

[7] Bunkei Matsushita, Wei Yang, Jin Chen, Yuyichi Onda, and Guoyu Qiu. Sensitivity of the Enhanced Vegetation Index (EVI) and Normalized Difference Vegetation Index (NDVI) to topographic effects: A case study in high-density cypress forest. *Sensors*, 7(11):2636–2651, 2007.

[8] Xiaolian Li, Weiguo Song, Liping Lian, and Xiaoge Wei. Forest fire smoke detection using back-propagation neural network based on MODIS data. *Remote Sensing*, 7(4):4473–4498, 2015.

[9] S. Veraverbeke, S. Lhermitte, W. W. Verstraeten, and R. Goossens. The temporal dimension of differenced Normalized Burn Ratio (dNBR) fire/burn severity studies: The case of the large 2007 Peloponnese wildfires in Greece. *Remote Sensing of Environment*, 114(11):2548–2563, 2010.

[10] Alberto G Villafranca, Jordi Corbera, Francisco Martín, and Juan Fernando Marchán. Limitations of Hyperspectral Earth Observation on Small Satellites. *Journal of Small Satellites*, 1(1):19–29, 2012.

[11] Lu Cheng. Personal communication, September 2020. Hamamatsu Corporation.

[12] CMV4000 - 4MP global shutter CMOS image sensor for machine vision — ams. https://ams.com/cmv4000. Accessed: 2021-05-25.

[13] Spectral Sciences Inc. Modtran demo. http://modtran.spectral.com/modtran_home. Accessed: 2021-05-25.

[14] Spectral Reflectance. http://gsp.humboldt.edu/OLM_2017/courses/GSP_216_Online/lesson2-1/reflectance.html. Accessed: 2021-05-25.

[15] R.R Auelmann. Image quality metrics.

[16] Wyvern. Personal communication, April 2021.

[17] MatWeb. Alclad aluminum 6061-t6, t651. http://www.matweb.com/search/GetReference.aspx?matid=9388. Accessed: 2021-06-01.

[18] L L C NanoRacks. NanoRacks CubeSat Deployer (NRCSD) Interface Definition Document (IDD) NRCSD List of Revisions. (Idd), 2013.

[19] James H. Burge. Mounting of optical components. https://wp.optics.arizona.edu/optomech/wp-content/uploads/sites/53/2016/08/26-Mounting-of-lenses-1.pdf. Accessed: 2021-06-01.

[20] Momentive Performance. Rtv556 technical data sheet. https://www.momentive.com/en-us/products/tds/rtv566?productid=d69e3b32-66e5-45c0-8e9c-9c2781aabe55. Accessed: 2021-06-01.

[21] Optical Research Associates. Design strength of optical glass. https://wp.optics.arizona.edu/optomech/wp-content/uploads/sites/53/2016/10/doyle-2003.pdf. Accessed: 2021-06-01.

[22] Brent Nicholas Anders Brakeboer. Development of the structural and thermal control subsystems for an earth observation microsatellite and its payload, msc thesis, university of toronto. 2015.